

# A Design of Hadronic Calorimeter for DarkSHINE Experiment\*

Zhen Wang,<sup>1,2,3</sup> Rui Yuan,<sup>1,2,3</sup> Hanqing Liu,<sup>2,3</sup> Jing Chen,<sup>2,3,1</sup> Xiang Chen,<sup>2,3</sup> Kim Siang Khaw,<sup>1,2,3</sup> Liang Li,<sup>2,3</sup> Shu Li,<sup>1,2,3</sup> Kun Liu,<sup>1,2,3</sup> Qibin Liu,<sup>1,2,3</sup> Siyuan Song,<sup>2,3,1</sup> Tong Sun,<sup>1,2,3</sup> Xiaolong Wang,<sup>4,5</sup> Yufeng Wang,<sup>1,2,3</sup> Haijun Yang,<sup>2,3,1</sup> Junhua Zhang,<sup>1,2,3</sup> Yulei Zhang,<sup>2,3</sup> Zhiyu Zhao,<sup>1,2,3</sup> Chunxiang Zhu,<sup>2,3,1</sup> Xuliang Zhu,<sup>1,2,3</sup> and Yifan Zhu<sup>2,3,1</sup>

<sup>1</sup>*Tsung-Dao Lee Institute, Shanghai Jiao Tong University, 1 Lisuo Road, Shanghai 201210, China*

<sup>2</sup>*Institute of Nuclear and Particle Physics, School of Physics and Astronomy, 800 Dongchuan Road, Shanghai 200240, China*

<sup>3</sup>*Key Laboratory for Particle Astrophysics and Cosmology (MOE),*

*Shanghai Key Laboratory for Particle Physics and Cosmology (SKLPPC),  
Shanghai Jiao Tong University, 800 Dongchuan Road, Shanghai 200240, China*

<sup>4</sup>*Key Laboratory of Nuclear Physics and Ion-beam Application (MOE), Fudan University, Shanghai 200443, China*

<sup>5</sup>*Institute of Modern Physics, Fudan University, Shanghai 200443, China*

The sensitivity of the dark photon search through invisible decay final states in low background experiments significantly relies on the neutron and muon veto efficiency, which depends on the amount of material used and the design of detector geometry. This paper presents an optimized design of a hadronic calorimeter (HCAL) used for the DarkSHINE experiment, which is studied using a GEANT4-based simulation framework. The geometry is optimized by comparing a traditional design with uniform absorbers to one that uses different thicknesses at different locations of the detector, which enhances the efficiency of vetoing low-energy neutrons at the sub-GeV level. The overall size and total amount of material used in HCAL are optimized to be lower due to the load and budget requirements, while the overall performance is studied to meet the physical objectives.

Keywords: Hadronic Calorimeter, GEANT4 Simulation, Neutron background, Scintillation Detector, Dark Photon

## I. INTRODUCTION

Over the past few decades, more and more astronomical observations have shown that there is not only ordinary matter in the universe that can be observed by electromagnetic interactions but also plenty of matter that does not interact with the electromagnetic force, which is so-called dark matter (DM) [1, 2]. One can predict that dark matter does not only interacts through the gravitational force but can also be studied as dark matter particles from the particle physics perspective. The research conducted from this perspective offers the mechanism to elucidate the evolutionary process of dark matter composition and investigates potential novel interactions between DM candidate particles and Standard Model (SM) particles.

Within a class of prevailing theories, a mechanism known as “freeze-out” [3] is introduced to elucidate the evolutionary process. The universe was in thermal equilibrium at the beginning of its existence, and dark matter was constantly being created and annihilated in pairs. As the universe subsequently underwent expansion and cooling, resulting in a greater dispersion of matter, the density of dark matter reached a steady state. “Freeze-out” allows for the existence of dark matter across a broad mass spectrum ranging from MeV to 10s TeV, and which can be further divided into Light Dark Matter (LDM) within the MeV to GeV mass range and Weakly Interactive Massive Particles (WIMP) within the

GeV to TeV mass range [4–10].

Searching for these dark matter particles is essential and challenging to elementary particle physics today. Among them, the search for WIMPs has been extensively explored for a long time. In general, the WIMP hypothesis provides a more natural and intuitive framework for the existence and detection of large mass but weakly interacting particles. Numerous experiments have obtained constraints on the mass of WIMPs [11], such as AMS [12], DAMPE [13], LHC [14], BESIII [15], Xenon [16], and PandaX [17]. These experiments encompass space experiments, collider experiments, and underground experiments, searching for WIMPs through direct exploration and indirect detection. So far, the limits on mass of WIMPs are close to the neutrino floor [18].

However, the current research on LDM remains insufficient, making it a prominent subject in recent investigations into dark matter. In the relevant beyond Standard Model theory of LDM, a particle analogous to an ordinary electromagnetic photon is introduced as a mediator for transporting interaction between dark matter, commonly referred to as the dark photon ( $A'$ ) [19, 20]. Moreover, the dark photon can be coupled to a SM photon via kinetic mixing ( $\epsilon$ ) and subsequently interact with SM particles. Dark photon plays a crucial role in mediating interactions between dark matter and ordinary matter [21–23]. Several international experiments, including NA64 [24], BESIII [25], and LDMX [26–28], are currently in operation or under development to search for dark photon.

The DarkSHINE experiment [29, 30] is a new initiative of fixed target experiment that utilizes an 8 GeV high repetition rate low-current electron beam, which will be provided

\* This work was supported by National Key R&D Program of China (Grant No.: 2023YFA1606904 and 2023YFA1606900), National Natural Science Foundation of China (Grant No.: 12150006), and Shanghai Pilot Program for Basic Research—Shanghai Jiao Tong University (Grant No.: 21TQ1400209).

by the future Shanghai High Repetition-Rate XFEL and Extreme Light Facility (SHINE) [31–33], and the primary goal is to search for dark photon through its invisible decays into dark matter particles. DarkSHINE is expected to exhibit sensitivity to dark photons within the mass range of MeV to GeV, according to predictions. The illustrative overview of the preliminary design for the DarkSHINE detector is shown in Figure 1, including Silicon Tracker, Electromagnetic Calorimeter (ECAL), and Hadronic Calorimeter (HCAL). The fixed tungsten target is placed in between the tagging and recoil trackers, immersed in the magnetic field.

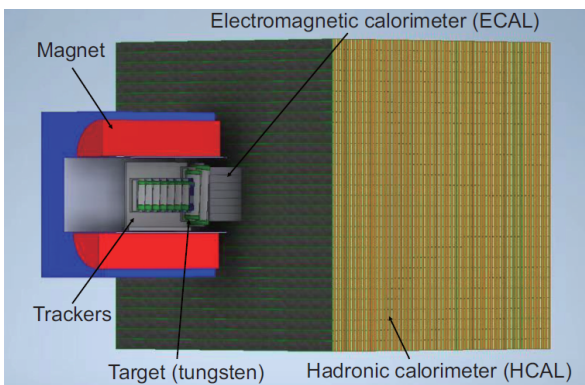


Fig. 1. Sketch picture of DarkSHINE detector. Electron incident direction is from left to right in the picture, Red material with a blue brace is the dipole magnet. The tagging tracker is placed at the center of it, while the recoil tracker is located at the edge of the magnet. The target is caught in the middle of the tracker. ECAL is placed after the tracker, followed by HCAL. [29]

The silicon tracker, immersed in the 1.5 T magnetic field generated by the magnet system, is used to reconstruct the trajectory of the incident and recoil electrons and to obtain the momentum of electrons. The tracker system includes a tagging tracker and a recoil tracker, and both are immersed in the magnetic field. The tagging tracker comprises seven silicon strip layers, while the recoil tracker has six. A tungsten (W) target is placed between these two parts of the tracker. The target has a decay length of  $0.1X_0$ . In each layer of the tracking module, two silicon strip sensors are placed at a small angle (100 mrad) to improve the position accuracy.

ECAL is placed after the recoil tracker and comprises 11 layers of crystal scintillator. Each layer includes  $20 \times 20$  LYSO (Ce) crystal scintillator, which has an area of  $2.5 \text{ cm} \times 2.5 \text{ cm}$  and a length of 4 cm. 11 layers can provide  $44 X_0$  of decay length. The design aims to effectively absorb all the energy of incoming electrons and photons, while utilizing crystals with excellent energy resolution to achieve optimal sensitivity. In addition to enabling more precise measurements of deposition energy, the combination of information captured by ECAL and tracker facilitates a comprehensive reconstruction of recoil electrons.

HCAL is a sampling calorimeter of “Fe-Sc” type, which

uses iron as the absorber layer and plastic scintillator strips to construct the sensitive layer. Each sensitive layer consists of two scintillator layers positioned between the two absorbers. The scintillator strips in the two layers are perpendicular to each other in the  $xy$  plane, as illustrated in Figure 2. The cross-sectional area of HCAL is  $4 \text{ m} \times 4 \text{ m}$ , and the length is also 4 m, in which these materials could provide more than  $10 \lambda$  of interaction length.

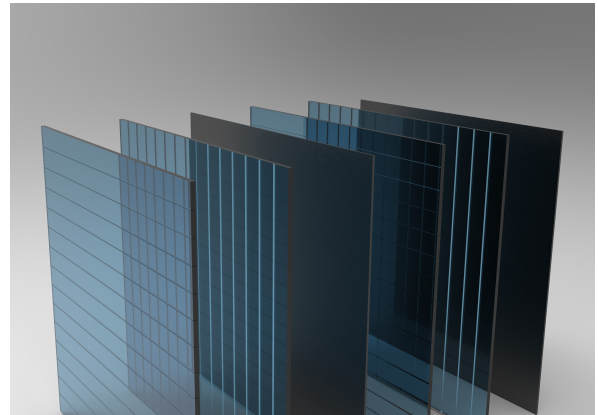


Fig. 2. Sketch map of the  $xy$ -crossing scintillator structures. Transparent parts are scintillator layers and the opaque parts are iron layers. One scintillator layer consists of  $x$ -direction sub-layer and  $y$ -direction sub-layer.

The interaction between the electron and the target is expected to produce dark photons, as illustrated in Figure 3. These dark photons carry a portion of the incident electron’s energy and subsequently decay into particles of dark matter, which then traverse the remaining detectors without leaving any discernible traces. Simultaneously, the residual energy is carried away by the recoil electron, traversing a path within the recoil tracker and subsequently being fully absorbed by the ECAL. In certain scenarios, the dark photon may exhibit a visible decay mode as well. The decay of the dark photon into a pair of Standard Model particles introduces an additional vertex containing  $\epsilon$ , resulting in a significantly suppressed cross section for this process compared to that of invisible decay [29]. In this invisible decay signal process, the energy difference between the incident energy and the deposited energy of the ECAL can be treated as the dark photon’s energy.

HCAL is designed to veto background events that exhibit similar behavior in tracker and ECAL as signal events. These events typically involve neutrons and muons, which can occur in both the target and ECAL area, resulting in minimal energy deposition in ECAL but detectable number of deposits in HCAL. Since ECAL acts as a fully absorbed calorimeter, neither the recoiled electrons nor the dark matter provide any discernible information in HCAL. Therefore, when HCAL registers a certain amount of deposited energy, it serves as a veto condition for this type of background scenario. As a low background experiment, the sensitivity of

the DarkSHINE is directly influenced by the power of HCAL to identify these events.

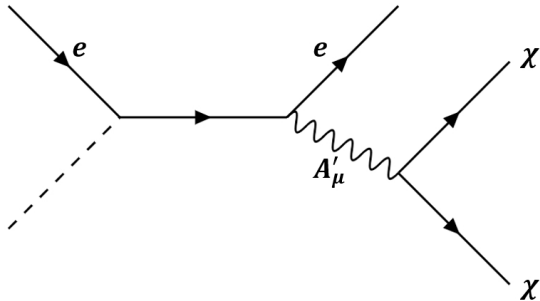


Fig. 3. The Feynman diagram illustrates the signal process in the DarkSHINE experiment, encompassing bremsstrahlung production and invisible decay of dark photons [29].

This paper presents the design and optimization of HCAL for DarkSHINE experiments. The primary criterion for evaluating optimization is the detector's capability to discern events containing neutrons, which are predominant in target particles and pose challenges for detection. The need for optimization mainly arises from budget constraints and building load considerations. It is necessary to reduce the weight of HCAL within a specific range while ensuring an adequate amount of materials are used and minimizing waste. The weight is dominated by iron, and the cost is mainly from the scintillator, which is directly related to the number of layers. The section II provides an overview of the background processes related to this optimization concern and discusses the criteria for optimization. Subsequently, sections III and IV present the details and results of the optimization, while section V concludes with a comprehensive summary.

## II. MAIN BACKGROUND IN HCAL AND TREATMENT

Mostly, beam electrons would pass through the tungsten target without any interaction, predominantly depositing the bulk of their energy in the ECAL in the form of electromagnetic shower. Rejection of these background events are straightforward; a cut-off based on the total energy accumulated in ECAL ( $E_{\text{ECAL}}$ ) could be employed since recoil electrons from signal processes are expected to possess lower deposited energies [29]. Additionally, a small fraction of electrons, however, generate an additional photon through the process of hard bremsstrahlung. These bremsstrahlung photons can either end in electromagnetic showers within ECAL and be vetoed using similar  $E_{\text{ECAL}}$  cut, or exhibit conversions into lepton or hadron pairs, which may occur within both the target and ECAL. In the context of electron pairs, events can be identified either in the tracker or/and ECAL, depending on the location of conversions.

The role of the HCAL is crucial in photons conversion into  $\mu$  pairs and hadron pairs [34]. Muons pass through the ECAL as minimum ionizing particles (MIP), which reduces the effectiveness of the  $E_{\text{ECAL}}$  cut. While the DarkSHINE ECAL has potential advantages in providing additional information such as tracks and topology within the ECAL, it is essential to emphasize that the information obtained from HCAL remains paramount and straightforward without requiring complex reconstruction algorithms. The situation is analogous for the final states of charged hadron pairs, where combining information from both ECAL and HCAL can lead to exclusion. However, in the case of neutral hadrons that do not decay within ECAL, discrimination power heavily relies on HCAL.

These bremsstrahlung photons can also interact with materials within the target and ECAL, resulting in photon-nuclear reactions that give rise to neutral hadrons. There exists a class of processes, which are significantly less frequent [34], exhibiting behavior similar to signal processes in the tracker and ECAL. In these cases, typically involving a single energetic ( $> 1$  GeV) neutral hadron. One can predict that a HCAL with sufficient absorber thickness could capture some of the shower energy and veto such events. Furthermore, electron-nuclear interactions with the materials of ECAL and target also involve nucleon production, and the treatment remains the same as for photon-nuclear processes.

A schematic representation of these processes described before is provided in Figure 4. The previously discussed backgrounds pertain to instrumental background, which impose limitations on the experiment's sensitivity due to their detection efficiency. Additionally, there exist irreducible physics backgrounds that encompass neutrino processes. However, these backgrounds exhibit a rate approximately four orders of magnitude [34] lower than the  $3 \times 10^{14}$  EOT and will not be addressed in this paper owing to their negligible impact.

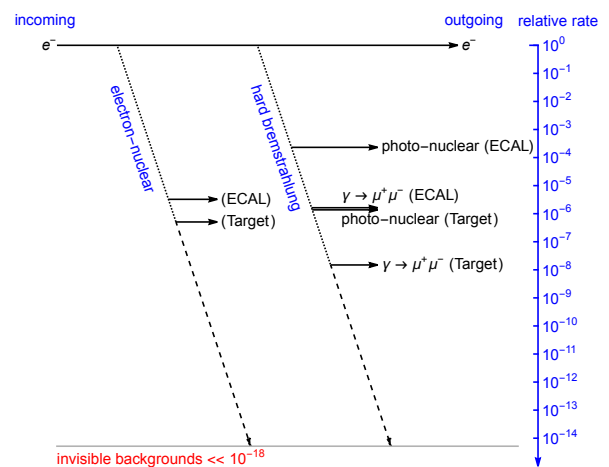


Fig. 4. Flow of background processes, ECAL and target refer to the locations where the processes occur.

Compared to neutral hadrons, muons are more straightforward to detect due to their significant energy deposit in enough layers of scintillators. The primary concern lies in the HCAL's capability of detecting neutral hadrons, as the veto power of hadronic particles becomes a crucial function and design consideration. These rare processes, such as photon-nuclear (PN) and electron-nuclear (EN) reactions, can be further categorized based on whether they occur in the target or ECAL. They are referred to as PN-target, PN-ECAL, EN-target, and EN-ECAL, respectively. Table 1 provides a proportion summary of the most frequently generated particles from these rare processes. Given that neutrons constitute the largest proportion and protons can be excluded through a combination of tracker and ECAL information, this study primarily utilized neutrons to validate the optimization effect, with all target particles being tested subsequently.

Table 1. Particle types and frequencies from electron-nuclear and photon-nuclear process, neutrons are predominant.

Process	Neutron	Proton	Pion	Kaon
Electron-Nuclear	73.42%	21.52%	4.64%	0.42%
Photon-Nuclear	64.95%	18.56%	14.43%	2.06%

HCAL rejects an event by setting cuts on the deposited energy of the neutrons in the event, and the efficiency of the veto varies for neutrons of different energies. Notably, the veto efficiency for a single-neutron event is identical to that of the neutron, while the efficiency of a multi-neutron event is tantamount to the veto efficiency of at least one of these neutrons. This veto performance is evaluated by a number defined as the ratio between the number of events (or neutrons) not being vetoed and the total number, referred to as veto inefficiency.

The energy distribution and number of neutrons in prediction events are studied and are illustrated in Figure 5. As discussed in section I, the ECAL of DarkSHINE absorbs all photon and electron energy, providing the total deposited energy quantity. The variable  $E_{\text{ECAL}}$  can effectively discriminate against numerous background events, as the majority of background events tend to exhibit higher values of  $E_{\text{ECAL}}$  compared to the signal. To specifically focus on events that cannot be rejected by other sub-detectors but rely on the rejection power of HCAL, only events satisfying the cut  $E_{\text{ECAL}} < 2.5$  GeV [29] are presented.

This study involves simulating  $1 \times 10^8$  electrons hitting the target. Considering that only a few or fewer neutrons survive in this phase space, it is expected that around  $1 \times 10^6$  energetic ( $> 1$  GeV) neutrons will be generated with the conditions of  $1 \times 10^{14}$  EOTs, which is consistent with the predicted number to be collected within one year [29]. Consequently, a veto inefficiency  $< 10^{-5}$  is chosen as the performance benchmark for high-energy neutron rejection, capable of reducing energetic neutrons to the unit level. Conversely, in the absence

of high-energy neutrons and presence of solely low-energy neutrons, it is implausible for these particles to be the sole particles detected in the event; otherwise, the ECAL would have recorded an energy deposition closer to 8 GeV. In such a scenario, a veto inefficiency  $< 10^{-3}$  would suffice to achieve equivalent rejection power if multiple neutrons are present.

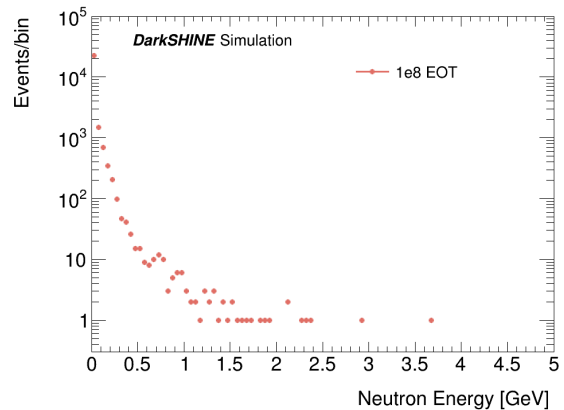


Fig. 5. Neutron energy distribution after applying cut on ECAL energy to request  $E_{\text{ECAL}} < 2.5$  GeV. The result shows that very few neutrons with energy greater than 1 GeV is left after ECAL cut. Which means under assumptions of  $1 \times 10^{14}$  EOTs, one can expect there to be at most  $1 \times 10^6$  level energetic neutrons.

### III. OPTIMIZATION OF THE DESIGN

#### A. Simulation introduction

The optimization study is conducted using the DarkSHINE software [29], a comprehensive simulation and analysis framework that seamlessly integrates various functions, such as detector simulation, electronic signal digitization, event display, event reconstruction, and data analysis. This all-in-one package, built upon GEANT4 v10.6.3 [35], is characterized by the DarkSHINE detector, and employs an internal data structure to facilitate efficient data flow across different stages.

GEANT4 is a comprehensive toolkit specifically designed for simulating the interaction of particles with matter, which plays a critical role in the development and optimization of HCAL. It is widely used in high energy physics analysis due to its extensive functionalities including particle tracking, detailed geometry configurations, sophisticated physics models, and particle hit detection. The toolkit supports a wide range of physics processes encompassing electromagnetic, hadronic, and optical interactions, and provides an extensive library of long-lived particles, materials, and elements across various energy spectra. GEANT4's architecture excels in managing complex geometries while offering flexibility for customization to meet the unique demands of scientific and engineering applications.



These properties of GEANT4 enable us to employ two different simulation strategies in this study. Firstly, the target particles are directly simulated to hit the HCAL without taking into account other detector components. This approach allows us to easily obtain large statistics and intuitively calculate the veto efficiency of the target particle (Section III). Secondly, the complete simulations are conducted to evaluate the veto efficiency of rare process events involving neutrons or muons by applying bias functions while electrons interact with the target and traverse all detectors. (Section IV). The absence of this bias function would result in excessive consumption of computing resources when simulating inclusive background instances until the statistics of certain rare process instances reach the required level.

As documented in Ref [29], the DarkSHINE experiment employs two cuts to veto the muons and hadronic particles, relying on the HCAL variables  $E_{\text{HCAL}}^{\text{total}}$  and  $E_{\text{HCAL}}^{\text{MaxCell}}$ . Here,  $E_{\text{HCAL}}^{\text{total}}$  represents the total energy collected in the HCAL, while  $E_{\text{HCAL}}^{\text{MaxCell}}$  corresponds to the highest energy deposition among all cells (scintillator strip). In this paper, considering the wide range of sizes tested, a scintillator unit width of 5 cm is chosen due to its small and easily divisible value.

The cut value has been optimized since its initial publication [29] to achieve an improved signal-to-background ratio, and is thereby adopted as the baseline selection criteria in this study:

- total energy reconstructed in HCAL,  $E_{\text{HCAL}}^{\text{total}} < 30 \text{ MeV}$ ;
- maximum cell energy in HCAL,  $E_{\text{HCAL}}^{\text{MaxCell}} < 0.1 \text{ MeV}$ .

To achieve a sufficiently accurate estimation to meet the requirement of  $< 10^{-5}$  veto inefficiency, the studies presented in this section employ  $10^6$  events for each test point (excluding section III E, in which the number is  $10^7$ ). In the corresponding plots, even if 0 out of  $10^6$  events survive the cuts, they are still counted as  $1 \times 10^{-6}$  veto inefficiency, identical to the scenario where 1 out of  $10^6$  events survives. This treatment is necessitated by the fact that the current number of simulated events cannot represent the scenario between 0 and  $1 \times 10^{-6}$  while maintaining the validity of the logarithmic axis.

## B. Transverse Size

The transverse dimensions of the HCAL, which determine its coverage angle, are crucial for effectively vetoing events with neutral particles and analyzing rare processes. The consideration of coverage angle encompasses not only the trajectories of secondary particles generated from electron-target interactions but also the dimensions of both electromagnetic and hadronic showers. In designing and optimizing the HCAL, a comprehensive range of factors

must be considered. While larger size offers benefits, there is a limit to its increase. Therefore, considering physical requirements along with budget costs and weight limitations imposed by experimental conditions becomes dominant. As a sampling calorimeter, it is not essential to capture the complete shower information; instead, it only requires sufficient components within the shower cluster to be deposited into the scintillator and subsequently vetoed by the designated selection criteria. Therefore, provided that the exclusion efficiency of the HCAL satisfies the criteria discussed in the Section II, opting for a smaller size would yield reduced budget and overall weight, thus constituting an optimal choice.

Worldwide, diverse detectors exist with varying coverage angles designed for specific purposes. Our methodology focuses on monitoring secondary particles projected forward in alignment with the beam's direction. By subjecting the HCAL to direct tests involving the injection of various particles, its performance can be independently evaluated since it serves as the final component of the detector. Given that the incident is a particle rather than a complete event, it is unnecessary to introduce screening information provided by other sub-detectors at this stage. This approach facilitates the accumulation of experience in HCAL design, rather than focusing on a highly specific case, and enables a comprehensive understanding of how the lateral size of the HCAL impacts the efficiency and effectiveness across various experimental scenarios.

This research meticulously explores the influence of varying transverse sizes on the veto capabilities of the HCAL, spanning dimensions from  $4 \text{ m} \times 4 \text{ m}$  [29] to the more compact  $1 \text{ m} \times 1 \text{ m}$  scale. Simulations were meticulously conducted for each specified transverse size, adhering to the methodological framework delineated in section III A. To comprehensively investigate the trends of variation, a range of particle energies spanning from 100 MeV to 3000 MeV and several size options were traversed. A pivotal aspect of the study is the maintenance of a constant total absorber thickness, precisely  $10\lambda$ , across all designs. This strategic decision is aimed at mitigating any potential biases that might arise from variations in the total detector thickness, thereby ensuring that the observed differences in veto capabilities can be attributed solely to the transverse dimensions.

The HCAL design under investigation comprises four strategically arranged modules in a two-by-two configuration. These modules are meticulously dimensioned to be half the length of the HCAL's transverse side, reflecting a deliberate design choice that effectively balances structural integrity and functional efficiency. Moreover, the scintillator strips, essential for detection capabilities, are designed with a length equivalent to half of the HCAL's transverse side while maintaining a consistent width of 5 cm. This specification ensures heightened sensitivity while keeping the detector size manageable. Furthermore, this modular design will facilitate future detector construction and installation processes,

including placement of readout electronics and design of support structures.

The outcomes of these simulations, illustratively presented in Figure 6, provide critical insights into the relationship between the HCAL's transverse size and its veto efficiency. The Y-axis represents the veto inefficiency, while each curve corresponds to a specific size choice, and the X-axis denotes the incident particle energy. Preliminary findings suggest that variations in transverse dimensions significantly impact the HCAL's ability to effectively veto background events.

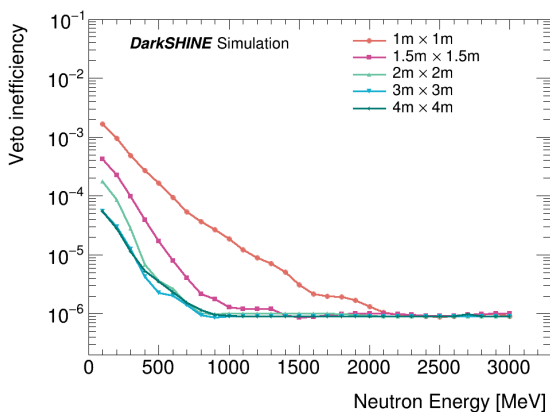


Fig. 6. Veto inefficiency as a function of different incident neutron energies. Larger size HCAL is showing better veto power as expected due to its capability of acceptance compared with smaller size HCAL designs. To satisfy the weighting limits of the SHINE facility, the 1.5 m design is selected to be the final choice.

In conclusion, these designs demonstrate equivalent veto power for high-energy neutrons in the energy range of 2 GeV to 3 GeV, while the performance of 1 m $\times$ 1 m design deteriorates significantly between 1 GeV and 2 GeV compared to the design above 1.5 m. For low-energy neutrons, larger area configurations offer enhanced performance. The veto inefficiency of low-energy neutrons in the 1.5 m $\times$ 1.5 m design is already below  $10^{-3}$ , which satisfies the specified requirement. Furthermore, the disparity in low-energy neutron veto between the 1.5 m and 1 m designs is more pronounced than that between the 4 m and 1.5 m designs. Given the SHINE facility's constraints on supporting structure and weight, a 1.5 m $\times$ 1.5 m design is selected to ensure sufficient interaction length while minimizing weight.

### C. Absorber thickness

Depending on the experimental design and the specific location of the detector within the overall experiment, there can be significant variations in the required information, leading to diverse approaches for designing the detector, even when employing identical materials. Among these, homogeneous

and sampling detectors stand out for their distinct design principles and applications. Homogeneous detectors are characterized by their uniform composition, utilizing a single material that simultaneously acts as both the active medium for detecting particles and the absorber. This design ensures a high resolution in measuring the energy of incoming particles, making homogeneous detectors particularly useful in environments where precision is paramount. On the other hand, sampling detectors are constructed from alternating layers of active and passive materials. The active layers are responsible for detecting particles, while the passive layers absorb them, allowing for the measurement of particle energies. Although sampling detectors may offer lower resolution compared to their homogeneous counterparts, they are highly valued for their efficiency and versatility in handling high-energy particles and complex events.

The DarkSHINE HCAL detector works as a sampling detector, capturing only a portion of the incoming energy in its sensitive layers. Consequently, an ideal absorber should be capable of capturing high-energy neutrons while retaining sufficient energy for low-energy neutrons to reach the scintillators. During this study, the hadronic veto system should effectively detect neutrons ranging from approximately 100 MeV to a few GeV. Low-energy neutrons would rapidly lose their energy within the absorbers, depositing minimal energy in the scintillator, while detectors might easily overlook high-energy neutrons if the absorber's thickness is inadequate.

The study simulates various absorber thicknesses within each detecting unit, ranging from 10 mm per layer to 100 mm per layer for different cases. The veto inefficiency as a function of detector depth is illustrated in figure 7, while the three plots represent the tests conducted with neutron injections at energies of 100, 500, and 2000 MeV, respectively. Each curve in these plots has a same number of test points representing the total absorber thickness from 100 mm to 1600 mm, incremented by 100 mm per step. The overall HCAL depth was used as the X-axis instead of the absorber thickness because it was easier to correspond the X-axis numbers to the overall HCAL dimensions.

The performance of a 10 mm absorber is optimal for 100 MeV neutrons, achieving a platform with approximately 70 layers. Both thick and thin absorbers can attain an inefficiency of  $<10^{-5}$  for high energy neutrons when provided with sufficient layers; however, a thicker absorber requires fewer layers when the depth remains constant. In order to understand these scenarios clearer, the veto inefficiencies as the function of detector depth for different beam energies, with two choices of thickness, 10 mm, and 50 mm, are shown in Figure 8. With an increased thickness of the absorber, it is feasible to reduce the number of layers and achieve an inefficiency of  $<10^{-5}$ , as demonstrated in the study.

One can obtain the conclusion that the new design for the DarkSHINE HCAL involves combining a thinner absorber in the front half of HCAL to collect deposit energy from low

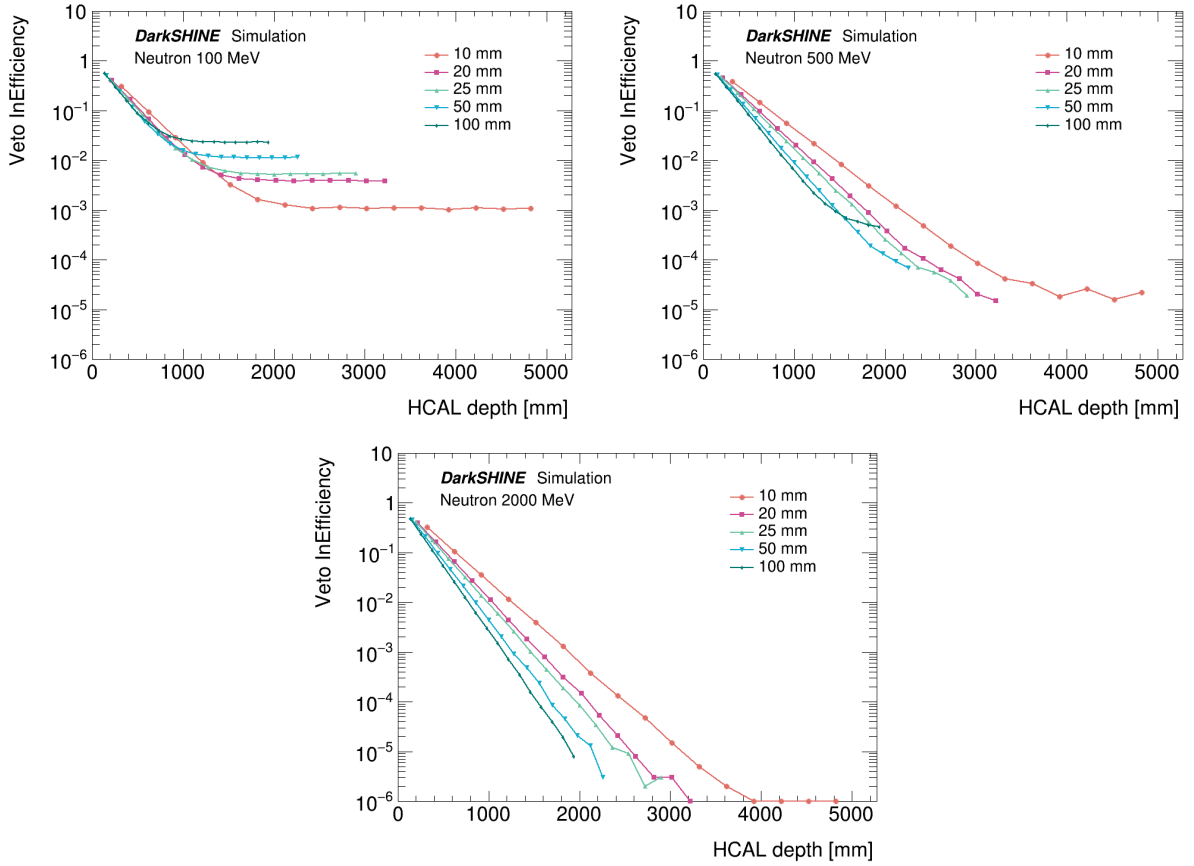


Fig. 7. Veto inefficiency as a function of detector depth for different absorber thickness. 100, 500 and 2000 MeV neutrons are generated to hit towards hadronic calorimeter at its center. The veto efficiency of low-energy neutrons can be enhanced in thinner absorber thickness, while thicker absorber thickness enables the vetoing of high-energy neutrons within a smaller depth range.

energy neutrons, and a thicker absorber in the remaining part to minimize the total material used. This approach employs 70 layers of 10 mm absorber and 18 layers of 50 mm absorber, which together achieve a total thickness of approximately  $10 \lambda$ , satisfying the physical requirements.

#### D. Scintillator layer design

The scintillator layer is composed of multiple scintillator strips, resulting in unavoidable gaps resembling a fence due to packaging and mechanical constraints. By rotating the second scintillator layer by 90 degrees, the orientation of the scintillator strips becomes orthogonal to those in the first layer, effectively complementing each other's gaps. The schematic representation of this basic structure is illustrated in Figure 2. However, it remains uncertain whether an intermediate structure between every two absorbers is necessary or if a single layer followed by an absorber would suffice.

The present study is conducted based on the results of the absorber thickness optimization presented in Section III C, in

which the initial 70 layers utilize a 10 mm absorber, followed by 50 mm layers. A comparison of veto inefficiencies is visualized in Figure 9. The default configuration involves the insertion of two 10 mm layers between each pair of absorbers, designated as 'xy-Abs-xy,' where 'xy' denotes the pair of scintillator layers and 'Abs' represents absorber. An alternative configuration is labeled 'x-Abs-y,' which signifies the insertion of an absorber layer between every two 10 mm scintillator layers with orthogonal strip direction. Furthermore, an additional comparison is made. The thickness of the scintillators is set at 20 mm.

All the configurations exhibit satisfactory performance for high-energy neutrons. For 100 MeV neutrons, a 10 mm thick x-Abs-y configuration exhibits slightly inferior performance, yet considering that the overall veto efficiency is the product of the inefficiencies of all particles in one event, it remains acceptable. The 20 mm thick x-Abs-y configuration demonstrates virtually identical performance to the xy-Abs-xy configuration, consistent with expectations but will not save any scintillator consumption. The x-Abs-y design with a 10 mm thick scintillator utilizes half the materials compared to the 20 mm configuration.

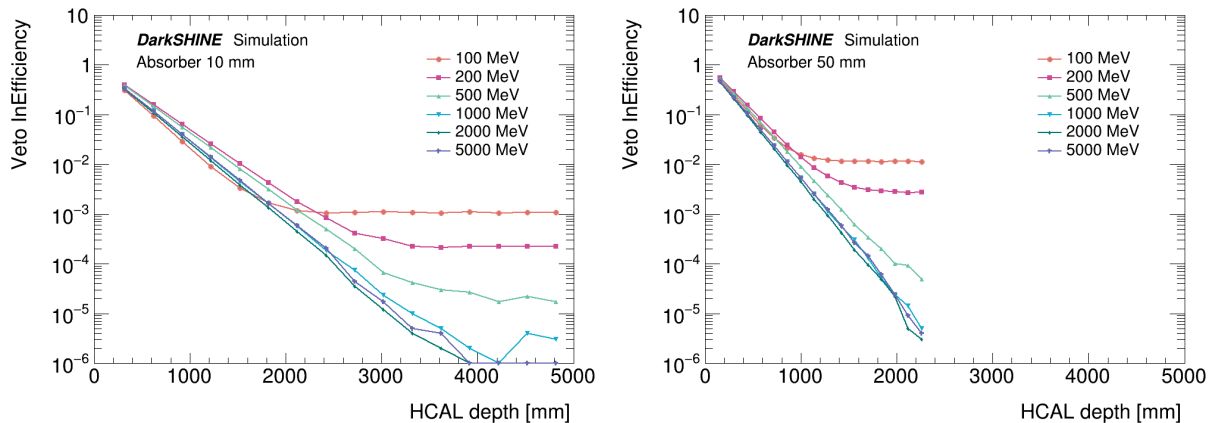


Fig. 8. Veto inefficiency as a function of detector depth for different beam energy. 10 mm and 50 mm absorber thickness results are shown, respectively. All the curves have same number of points, and the corresponding points in two plots represent same total absorber thickness but different HCAL depth.

### E. Optimization performance

As stated in Section II, the previous study utilized neutron veto inefficiency as the primary research indicator; however, it is imperative to evaluate the performance of all relevant particles entering HCAL. Veto inefficiency of various hadronic particles traversing through the optimized DarkSHINE HCAL is assessed by simulating different incident particles with distinct energies. The number of events is raised to  $10^7$ , and the test is conducted on neutron,  $k^0$  (both short- and long-lived),  $\pi^0$ , and proton. The result is shown in Table 2.

The HCAL demonstrates a nuanced performance gradient in its veto capabilities, particularly evident when examining its interaction with neutrons of disparate energies. Initial observations reveal that neutrons at the lower energy spectrum, approximately 100 MeV, are predominantly absorbed within the first few calorimeter's absorber layers. This absorption effectively precludes the generation or detection of secondary particles by the HCAL's sensitive layers. Such phenomena underscore the challenges inherent in detecting lower-energy neutrons due to their minimal interaction with the detector materials.

As we progress to a higher energy threshold, specifically around 500 MeV, there is a notable decrease in veto inefficiency. This decrease is indicative of the HCAL's enhanced capability to effectively identify and veto neutron events, aligning with the theoretical predictions and design objectives. The underlying mechanism facilitating this improved performance likely relates to the increased production of secondary particles and their subsequent energy deposition within the sensitive layers of the HCAL, thereby enabling more efficient detection and vetoing of the incident neutrons.

Advancing further into the energy scale, particularly in the realms exceeding 1000 MeV, the HCAL showcases a consistently low veto inefficiency across a broad array of hadronic particles, including but not limited to neutrons, kaons, and pions. The inefficiencies observed for these particles generally reside within the order of magnitude of  $10^{-5}$ , illuminating the HCAL's superior discrimination capabilities against higher-energy hadronic particles. This enhanced performance can be attributed to the calorimeter's design optimizations, which are specifically tailored to maximize its sensitivity and specificity in the higher energy domain.

Moreover, the differential behavior exhibited by various particle types within the HCAL elucidates the complex interaction between particles and detector materials. The variability in veto inefficiency among different hadrons is reflective of their distinct interaction mechanisms within the calorimeter, highlighting the sophisticated nature of the HCAL's operational parameters. These findings not only validate the efficacy of the optimized HCAL design in meeting the DarkSHINE experiment's stringent requirements but also contribute valuable insights into the fundamental aspects of particle detection and background event mitigation in high-energy physics research.

Table 2. Veto inefficiency of HCAL targeting different incident hadronic particles with different energies. Events with multiple hadronic particles could be more easily vetoed by HCAL detector under assumptions that veto power of different particles at one event is independent.

Particle \ Energy	n	$k^0$	$\pi^0$	p	$\mu$
100[MeV]	1.17E-03	3.16E-02	7.30E-06	3.07E-02	4.09E-04
500[MeV]	1.84E-05	5.40E-06	1.00E-07	8.04E-06	1.50E-05
1000[MeV]	3.70E-06	3.70E-06	1.00E-07	1.00E-07	2.00E-06
2000[MeV]	2.70E-06	1.15E-05	1.00E-07	1.00E-07	1.00E-07



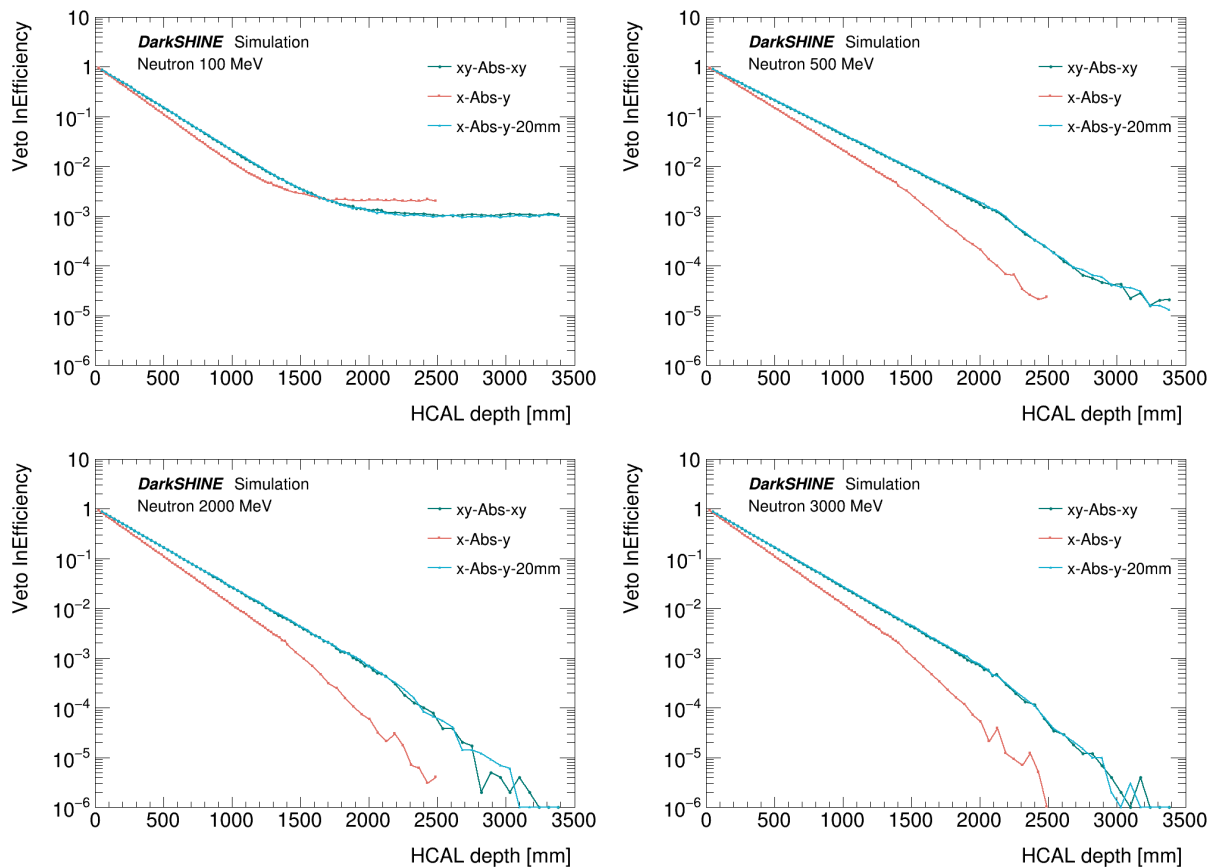


Fig. 9. Veto inefficiency as a function of detector depth for different absorber thicknesses and scintillator strategy. 100, 500, 2000, and 3000 MeV neutrons are generated to hit towards hadronic calorimeter at its center. 10 mm and 50 mm absorbers are used in the first 70 layers and the rest part, respectively. 20 mm-scintillator in x-Abs-y design shows roughly the same performance as 10 mm-scintillator in xy-Abs-xy design, while 10 mm-scintillator in x-Abs-y design performs slightly worse in low-energy scheme but reduce the amount of scintillator a lot.

#### IV. SIDE HCAL DESIGN

The optimization and validation of the target particle rejection power have been demonstrated, and this power is equivalent to the rejection power of background events where particles are incident upon the HCAL. However, not all occur within this context. Particles can exit from the ECAL via alternative paths and fail to enter the HCAL. In the rare processes discussed in section II, events may involve secondary particles with substantial azimuthal angles relative to the beam line. These processes, such as photon-nuclear and electron-nuclear interactions, can occur at various locations within the detector system. Secondary particles emitted from these interactions might be overlooked if the detector is unable to cover a specific solid angle.

Therefore, an additional segmented HCAL, referred to as the side HCAL, is incorporated. The side HCAL consists of four cuboid parts that encircle and envelope the ECAL end to end, with its sensitive surface being perpendicular to the ECAL. The proposed structure's width is envisioned to align with the ECAL's depth in the z direction, while its length

(in either x or y direction) would correspond to the sum of ECAL's width and half of the difference between HCAL's transverse size and ECAL's lateral length, representing the distance from one side of ECAL to the furthestmost side of HCAL.

Side HCAL is also composed of multiple iron absorber layers and plastic scintillator layers, each with an area of  $45\text{ cm} \times 105\text{ cm}$ , which is correlated to the ECAL dimensions [29]. Owing to the non-square layer shape, the 'x-y' design would result in differently sized scintillator strips and is thus not employed. Furthermore, an uneven absorber thickness is superfluous as the depth is significantly smaller than the main body. Each sensitivity layer and absorber layer is 10 mm thick, collectively consisting of 50 layers.

The performance of two designs, with and without a side HCAL, has been evaluated separately. Simulated events of four types of rare processes are employed to investigate the veto inefficiency. At this stage, the combination of the optimized designs discussed in our paper has been implemented, with no additional sub-detector cuts employed. These numbers should not be considered as a comprehensive

measure of the DarkSHINE experiment's veto inefficiency in excluding rare process events, but rather serve as a means to explore additional related events for comparative analysis within this specific context. The results are presented in Table 3, indicating that the inclusion of a side HCAL significantly enhances the overall performance.

Table 3. Veto inefficiency by simulating 8-GeV electron-on-target events into different structures and with different rare process biased. From the numbers, designs with side HCAL has better veto power than designs without side HCAL.

Structure \ Process	EN-target	EN-ECAL	PN-target	PN-ECAL
w/o Side HCAL	2.68E-02	3.94E-02	9.29E-02	1.24E-01
w/ Side HCAL	1.04E-03	1.09E-02	1.94E-03	3.58E-02

## V. CONCLUSION

The design and optimization of the hadronic calorimeter for the DarkSHINE experiment have been meticulously conducted. Factors such as the thickness of the absorber, the placement of scintillator, and the requirements of the side HCAL, which could influence the veto performance, have been thoroughly investigated. Several crucial parameters have been identified for optimization, taking into account

constraints such as limited weighting and budget conditions, which also satisfy the physical requirements.

In the optimized design, the HCAL consists of iron absorber layers and scintillator sensitive layers. The transverse dimensions are 1.5 m  $\times$  1.5 m, with approximately 10  $\lambda$  thick iron absorbing layers along the beam direction. The first 70 layers have a thickness of 1 cm, while the last 18 layers are 5 cm thick. Following each absorber, there is a 1 cm thick plastic scintillator layer composed of a strip measuring 5cm in width. The orientation of the scintillator strips in the two adjacent layers before and after an absorber layer is perpendicular to each other. Additionally, there is also a scintillator layer positioned between the ECAL and first iron layer. Apart from the main HCAL, a side HCAL surrounding the ECAL has been incorporated.

The novel design of HCAL offers enhanced veto power towards various rare processes, including electron-nuclear and photon-nuclear reactions, in particular those with neutral hadrons and muons in the decay final states. This optimized HCAL design will not only be crucial for the DarkSHINE experiment, but also demonstrate the importance of the advanced hadronic calorimetry techniques in particle physics experiments of such kind in general.

## VI. BIBLIOGRAPHY

- 
- [1] D. Hooper, D. P. Finkbeiner and G. Dobler, Possible evidence for dark matter annihilations from the excess microwave emission around the center of the Galaxy seen by the Wilkinson Microwave Anisotropy Probe. *Phys. Rev. D* **76** (2007), 083012. doi:10.1103/PhysRevD.76.083012, [arXiv:0705.3655 [astro-ph]].
- [2] D. Clowe, M. Bradac, A. H. Gonzalez *et al.*, A direct empirical proof of the existence of dark matter. *Astrophys. J. Lett.* **648** (2006), L109-L113. doi:10.1086/508162, [arXiv:astro-ph/0608407 [astro-ph]].
- [3] Y. Du, F. Huang, H. L. Li *et al.*, Revisiting dark matter freeze-in and freeze-out through phase-space distribution. *JCAP* **04** (2022) no.04, 012. doi:10.1088/1475-7516/2022/04/012
- [4] K. Griest and M. Kamionkowski, Unitarity Limits on the Mass and Radius of Dark Matter Particles. *Phys. Rev. Lett.* **64** (1990), 615. doi:10.1103/PhysRevLett.64.615
- [5] C. M. Ho and R. J. Scherrer, Limits on MeV Dark Matter from the Effective Number of Neutrinos. *Phys. Rev. D* **87** (2013) no.2, 023505. doi:10.1103/PhysRevD.87.023505, [arXiv:1208.4347 [astro-ph.CO]].
- [6] G. Steigman, Equivalent Neutrinos, Light WIMPs, and the Chimera of Dark Radiation. *Phys. Rev. D* **87** (2013) no.10, 103517. doi:10.1103/PhysRevD.87.103517, [arXiv:1303.0049 [astro-ph.CO]].
- [7] C. Boehm, M. J. Dolan and C. McCabe, A Lower Bound on the Mass of Cold Thermal Dark Matter from Planck. *JCAP* **08** (2013), 041. doi:10.1088/1475-7516/2013/08/041, [arXiv:1303.6270 [hep-ph]].
- [8] K. M. Nollett and G. Steigman, BBN And The CMB Constrain Light, Electromagnetically Coupled WIMPs. *Phys. Rev. D* **89** (2014) no.8, 083508. doi:10.1103/PhysRevD.89.083508, [arXiv:1312.5725 [astro-ph.CO]].
- [9] K. M. Nollett and G. Steigman, BBN And The CMB Constrain Neutrino Coupled Light WIMPs. *Phys. Rev. D* **91** (2015) no.8, 083505. doi:10.1103/PhysRevD.91.083505, [arXiv:1411.6005 [astro-ph.CO]].
- [10] P. D. Serpico and G. G. Raffelt, MeV-mass dark matter and primordial nucleosynthesis. *Phys. Rev. D* **70** (2004), 043526. doi:10.1103/PhysRevD.70.043526, [arXiv:astro-ph/0403417 [astro-ph]].
- [11] J. Liu, X. Chen and X. Ji, Current status of direct dark matter detection experiments. *Nature Phys.* **13** (2017) no.3, 212-216. doi:10.1038/nphys4039, [arXiv:1709.00688 [astro-ph.CO]].
- [12] F. Giovacchini *et al.* [AMS-02 RICH], The AMS-02 RICH detector: Status and physics results. *Nucl. Instrum. Meth. A* **952** (2020), 161797. doi:10.1016/j.nima.2019.01.024
- [13] D. Kyratzis [DAMPE], Results overview from the DAMPE space mission in orbit. *PoS PANIC2021* (2022), 310, doi:10.22323/1.380.0310
- [14] J. K. Behr, Searches for dark matter with the ATLAS and CMS experiments using LHC run 2 (2015-2018) data. *Proceedings of the 22nd Particles and Nuclei International Conference,*

- 2021.
- [15] V. Prasad [BESIII], Dark matter/ new physics searches at BESIII. PoS **ALPS2019** (2020), 030. doi:10.22323/1.360.0030, [arXiv:1907.12058 [hep-ex]].
- [16] E. Aprile *et al.* [XENON], Dark Matter Search Results from a One Ton-Year Exposure of XENON1T. Phys. Rev. Lett. **121** (2018) no.11, 111302. doi:10.1103/PhysRevLett.121.111302, [arXiv:1805.12562 [astro-ph.CO]].
- [17] Y. Meng *et al.* [PandaX-4T], “Dark Matter Search Results from the PandaX-4T Commissioning Run. Phys. Rev. Lett. **127** (2021) no.26, 261802. doi:10.1103/PhysRevLett.127.261802, [arXiv:2107.13438 [hep-ex]].
- [18] J. Billard, M. Boulay, S. Cebrián *et al.*, Direct detection of dark matter—APPEC committee report\*. Rept. Prog. Phys. **85** (2022) no.5, 056201. doi:10.1088/1361-6633/ac5754, [arXiv:2104.07634 [hep-ph]].
- [19] B. Holdom, Two  $U(1)$ 's and Epsilon Charge Shifts. Phys. Lett. B **166** (1986), 196-198. doi:10.1016/0370-2693(86)91377-8
- [20] R. Foot and X. G. He, Comment on  $Z$   $Z$ -prime mixing in extended gauge theories. Phys. Lett. B **267** (1991), 509-512. doi:10.1016/0370-2693(91)90901-2
- [21] K. Fuyuto, X. G. He, G. Li and M. Ramsey-Musolf, CP-violating Dark Photon Interaction. Phys. Rev. D **101** (2020) no.7, 075016. doi:10.1103/PhysRevD.101.075016, [arXiv:1902.10340 [hep-ph]].
- [22] G. Choi, T. T. Yanagida and N. Yokozaki, A model of interacting dark matter and dark radiation for  $H_0$  and  $\sigma_8$  tensions. JHEP **01** (2021), 127. doi:10.1007/JHEP01(2021)127, [arXiv:2010.06892 [hep-ph]].
- [23] Y. Cheng, X. G. He, M. J. Ramsey-Musolf *et al.*, CP-violating dark photon kinetic mixing and type-III seesaw model. Phys. Rev. D **105** (2022) no.9, 095010. doi:10.1103/PhysRevD.105.095010, [arXiv:2104.11563 [hep-ph]].
- [24] Y. M. Andreev *et al.* [NA64], Phys. Rev. Lett. **131** (2023) no.16, 161801 doi:10.1103/PhysRevLett.131.161801 [arXiv:2307.02404 [hep-ex]].
- [25] Y. Zhang, W. T. Zhang, M. Song, X. A. Pan, Z. M. Niu and G. Li, Phys. Rev. D **100** (2019) no.11, 115016 doi:10.1103/PhysRevD.100.115016 [arXiv:1907.07046 [hep-ph]].
- [26] T. Åkesson *et al.* [LDMX], Light Dark Matter eXperiment (LDMX). [arXiv:1808.05219 [hep-ex]].
- [27] T. Åkesson *et al.* [LDMX], A High Efficiency Photon Veto for the Light Dark Matter eXperiment. JHEP **04** (2020), 003, doi:10.1007/JHEP04(2020)003 [arXiv:1912.05535 [physics.ins-det]].
- [28] A. Berlin, N. Blinov, G. Krnjaic *et al.*, Dark Matter, Millicharges, Axion and Scalar Particles, Gauge Bosons, and Other New Physics with LDMX. Phys. Rev. D **99** (2019) no.7, 075001. doi:10.1103/PhysRevD.99.075001, [arXiv:1807.01730 [hep-ph]].
- [29] J. Chen, J. Y. Chen, J. F. Chen *et al.*, Prospective study of light dark matter search with a newly proposed DarkSHINE experiment. Sci. China Phys. Mech. Astron. **66**, no.1, 211062 (2023). doi:10.1007/s11433-022-1983-8
- [30] S. Li, Dark SHINE — a Dark Photon search initiative at SHINE facility. Proceeding for 31st International Symposium on Lepton Photon Interactions at High Energies. doi:10.5281/zenodo.8373963
- [31] J. Wan, Y. Leng, B. Gao, F. Chen *et al.*, Simulation of wire scanner for high repetition free electron laser facilities. Nucl. Instrum. Meth. A **1026**, 166200 (2022). doi:10.1016/j.nima.2021.166200
- [32] Z. T. Zhao, C. Feng and K. Q. Zhang, Two-stage EEHG for coherent hard X-ray generation based on a superconducting linac. Nucl. Sci. Tech. **28**, no.8, 117 (2017). doi:10.1007/s41365-017-0258-z
- [33] Z. T. Zhao, C. Feng, J. H. Chen *et al.*, Two-beam based two-stage EEHG-FEL for coherent hard X-ray generation. Science Bulletin **61**, 117 (2016), 720-727. doi:10.1007/s11434-016-1060-8
- [34] T. Åkesson *et al.* [LDMX], Photon-rejection power of the Light Dark Matter eXperiment in an 8 GeV beam. JHEP **12** (2023), 092. doi:10.1007/JHEP12(2023)092, [arXiv:2308.15173 [hep-ex]].
- [35] S. Agostinelli *et al.* [GEANT4], GEANT4—a simulation toolkit. Nucl. Instrum. Meth. A **506** (2003), 250-303. doi:10.1016/S0168-9002(03)01368-8